Atomically dispersed Ni active sites on covalent organic frameworks for heterogeneous metallaphotocatalytic C–N cross-coupling

Zhuwei Li [a,1], Yaning Li [b,1], Huijie Cheng [a], Yurou Song [a], Yuye Jiao [a], Shaobo Shi [a], Junfeng Gao [b], Licheng Sun [c,d], Jungang Hou [a,*]

[a] *State Key Laboratory of Fine Chemicals, Frontiers Science Center for Smart Materials Oriented Chemical Engineering, School of Chemical Engineering, Dalian University of Technology, Dalian 116024, PR China*
[b] *State Key Laboratory of Structural Analysis, Optimization and CAE Software for Industrial Equipment, Dalian University of Technology, Dalian 116024, PR China*
[c] *Center of Artificial Photosynthesis for Solar Fuels and Department of Chemistry, School of Science, Westlake University, Hangzhou 310024, PR China*
[d] *Department of Chemistry, School of Engineering Sciences in Chemistry, Biotechnology and Health, KTH Royal Institute of Technology, Stockholm 10044, Sweden*

ARTICLE INFO

ABSTRACT

Covalent organic frameworks (COFs) have been acknowledged as a potential platform for heterogeneous photoredox cross-coupling due to their excellent chemical stability, admirable controllability, and extremely prominent surface area. However, synthesizing COFs with bidentate ligand units and utilizing active sites remain a grand challenge. Herein, we report a promising new family of 2,6-pyridinedicarboxaldehyde-bis-(p-aminophenylimine)-based two-dimensional (2D) COFs (PP-COF) using an amine monomer and classic tri-aldehydes. On this basis, dispersed Ni single-atom sites were immobilized on three-types imine-based bi-coordinated 2D COFs (Ni SAS-PP-COF) as heterogeneous dual photoredox catalysts for photo/Ni dual-catalyzed C–N cross-coupling between aryl bromides and alkyl/sulfo amines. Under solar energy irradiation, PP-COF could absorb light to generate electrons and holes, then the photogenerated electrons are transferred to Ni sites to reduce divalent nickel to monovalent nickel. Monovalent nickel is necessary to drive the nickel catalytic cycle. Due to the increased charge separation and abundant active sites, the state-of-the-art Ni SAS-PP-COFs catalyst achieves excellent catalytic performance in comparison of pristine PP-COF. The heterogeneous Ni SAS-PP-COF catalytic system not only confirms the prospect of COFs as potential photoredox/transition-metal dual catalysts, but also provides in-depth insights into the synthesis of functional COFs toward practical metallaphotocatalytic application.

1. Introduction

Covalent organic frameworks (COFs) as extended structures with building blocks connected by covalent bonds, have garnered significant attention in recent decades due to their unique features such as periodic structure, large surface area, and excellent stability [1–7]. These properties make COFs an incredibly valuable platform for various potential applications, including molecular sensing [8,9], gas storage and separation [10–13], optoelectronics [14–16], energy storage [17–19], proton conductivity [20–22], and heterogeneous catalysis [23–29]. Despite widespread use in various applications, COFs have yet to fully exploit their potential in photocatalytic organic conversion. Enlightened by the above analysis, it is highly desirable to produce functional COFs with rational building units.

The development of multifunctional COFs is expedited by utilizing the well-established techniques of organic synthesis that guarantee precision in design [30–33]. A commonly used approach to generate COFs with particular functions is to incorporate functional moieties during polycondensation [34]. To date, a number of COFs with the specific geometric and chemical structures have been produced by the incorporation of appropriate ligands [35–40]. Meanwhile, the precise integration of single atoms and COFs with a well-defined coordination environment can create plentiful active sites in COFs, facilitating charge separation and thus promoting metallaphotocatalytic conversion [41–44]. However, the synthesis of bi-coordinated COFs that can be applied in photo/Ni dual-catalyzed cross-coupling reactions remains a
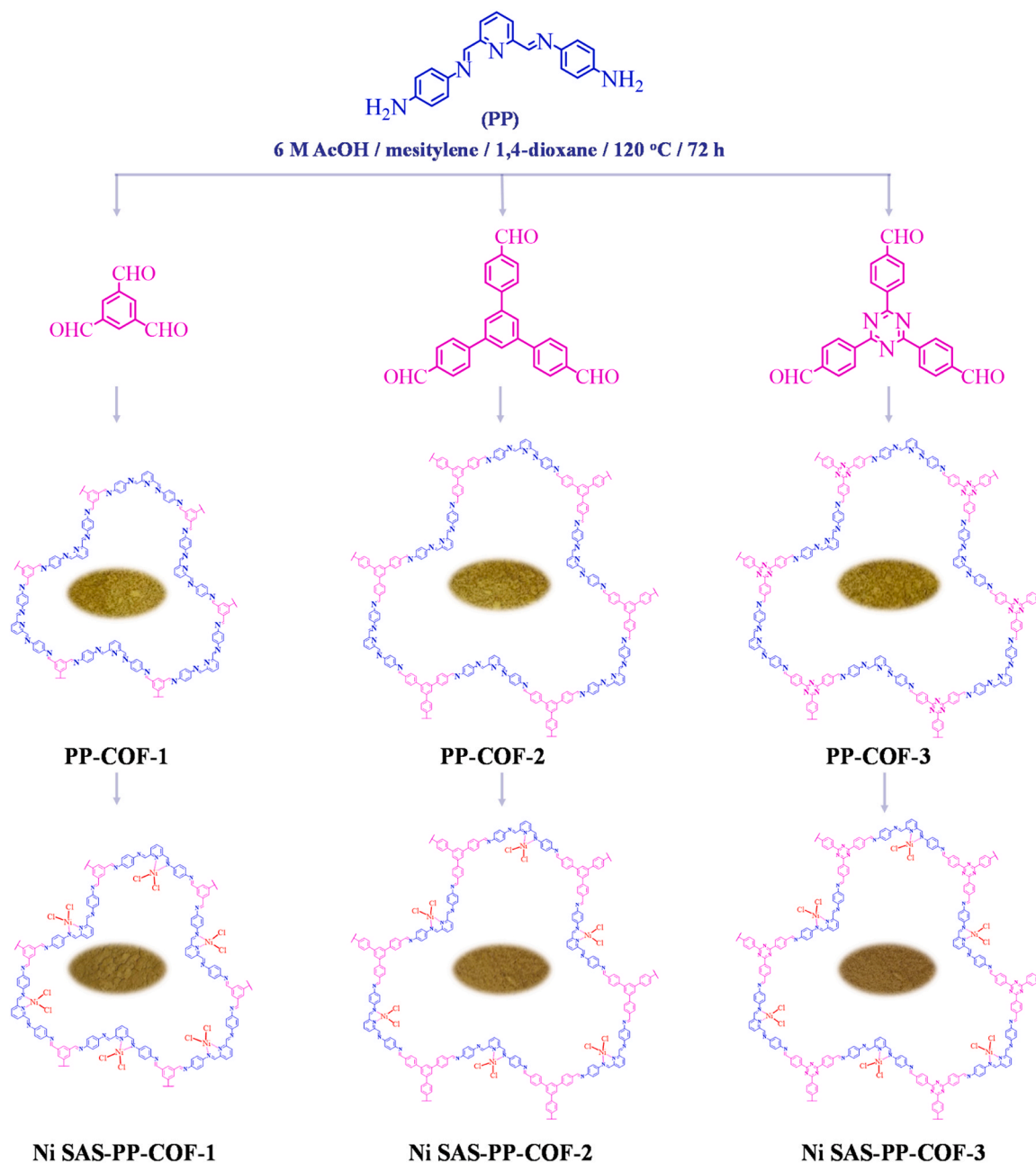
Fig. 1. Illustration of the synthesis of two-dimensional COFs (PP-COF) using an amine monomer and classic tri-aldehydes.

challenge, as such COFs have been rarely reported. In view of elucidating the atomic-level the correlation among suitable linkages and active sites of COFs and photoconversion, it is obligatory to develop a promising COFs catalyst with a well-defined coordination environment.

Heterogeneous catalysts for photocatalytic organic conversions have attracted extensive attention, with a particular emphasis on photo/Ni dual-catalyzed cross-coupling reactions [45–48]. Metal-organic frameworks (MOFs) [49], metal-organic layers (MOLs) [50], carbon nitride [51–53], sulfide quantum dots [54], and perovskite photocatalysts [55] have been applied in these reactions. Especially, the combination of COFs and single-atomic metal active sites by the construction of C–C [56], C–N [36,46], C–O [45], and C–S [48] bonds has been proven for heterogeneous photo/Ni dual-catalyzed cross-coupling reactions. However, the coordination of COFs with transition metal atoms for C–N bond coupling reactions is still a rare occurrence, posing a significant challenge for the precise design of COFs with superior performance.

Herein, we report a promising family of imine-based two-

dimensional (2D) COFs (PP-COF) using an amine monomer and classic tri-aldehydes. On this basis, dispersed Ni single-atom sites were immobilized on three-types 2,6-pyridinedicarboxaldehyde-bis-(p-aminophenylimine)-based bi-coordinated 2D COFs (Ni SAS-PP-COF) as heterogeneous dual photoredox catalysts by the evidence of synchrotron-radiation based X-ray absorption fine-structure spectroscopy and aberration-corrected high-angle annular dark-field scanning transmission electron microscopy (HAAF-STEM) for photo/Ni dual-catalyzed C–N cross-coupling between aryl bromides and alkyl/sulfo amines. Under solar energy irradiation, PP-COF could absorb light to generate electrons and holes, then the photogenerated electrons are transferred to Ni sites to drive the metallaphotocatalysis reaction. Due to the increased charge separation and abundant active sites from experimental analysis and density functional theory calculations, this state-of-art Ni SAS-PP-COF dual-photoredox system demonstrates significant functional group tolerance and high yield (79–97%) in comparison to pristine PP-COF.
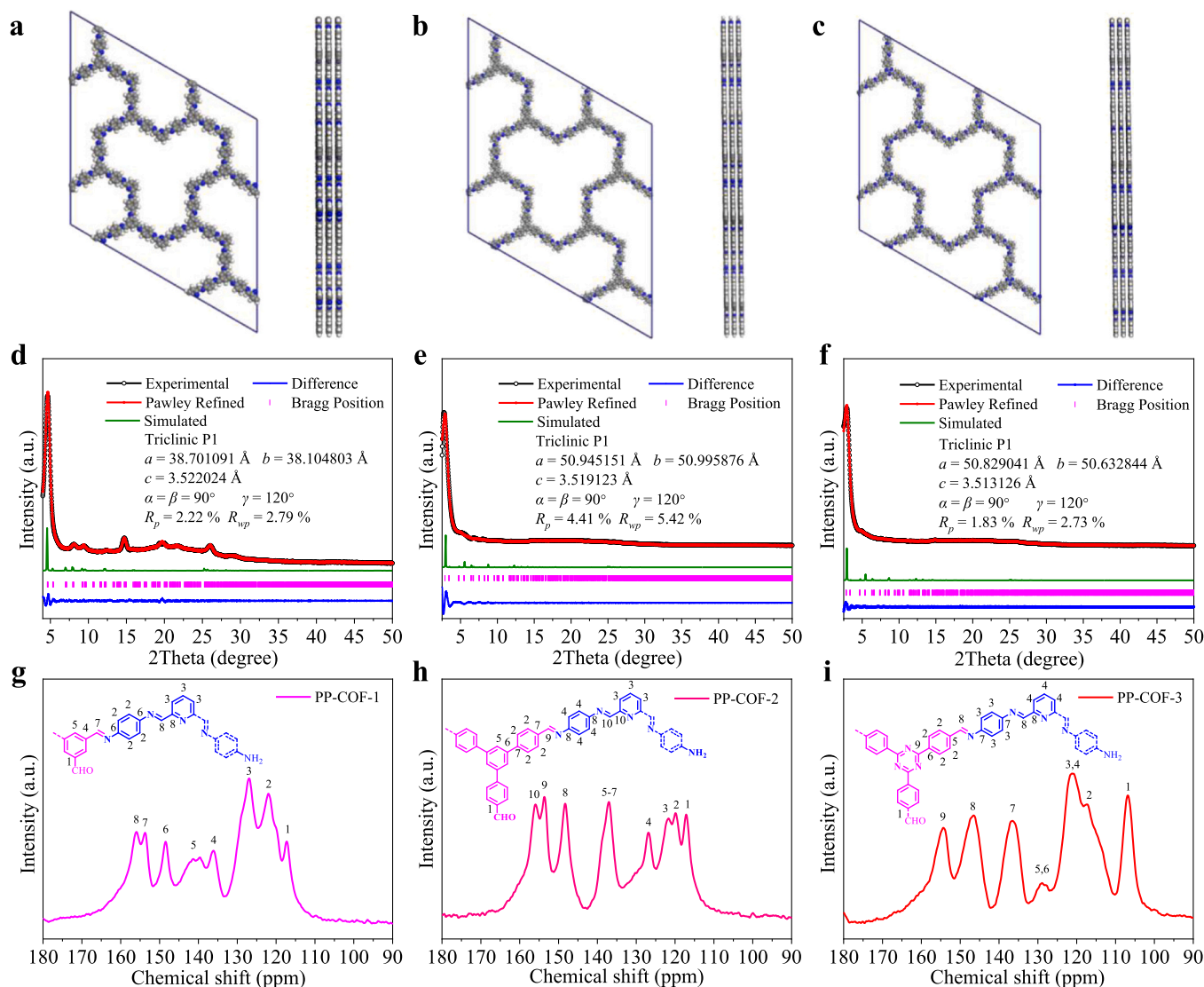
Fig. 2. Structural models of (a) PP-COF-1, (b) PP-COF-2 and (c) PP-COF-3 with eclipsed AA stacking patterns. PXRD patterns of (d) PP-COF-1, (e) PP-COF-2 and (f) PP-COF-3 with the experimental data in black, Pawley-refined data in red, Simulated data in dark green, Bragg positions in pink and the differences in blue. ^{13}C (CP/MAS) NMR spectra of (g) PP-COF-1, (h) PP-COF-2 and (i) PP-COF-3.

2. Experimental

2.1. Synthesis of PP-COFs

1,3,5-benzenetricarboxaldehyde (40.5 mg, 0.25 mmol) and 2,6-pyridinedicarboxaldhydebis-(p-aminophenylimine) (118.3 mg, 0.375 mmol) were dissolved in a mixture of mesitylene (1.8 mL) and 1,4-dioxane (10.2 mL) in a 50 mL vial. Then, 0.4 mL of 6 M acetic acid was added, and the vial was frozen and degassed using three freeze-thaw cycles. The vial was then kept at 120 °C for 3 days. The obtained precipitate was washed with tetrahydrofuran and methanol, and product was obtained by vacuum drying overnight (noted as PP-COF-1). Using the same procedure, Other photocatalysis were obtained using different tri-aldehyde monomers, i.e., 1,3,5-tris(4-formylphenyl)benzene and 4,4',4''-(1,3,5-triazine-2,4,6-triyl)tris[benzaldehyde] (noted as PP-COF-2 and PP-COF-3, respectively).

2.2. Synthesis of Ni SAS-PP-COFs

Different molar ratios of NiCl$_2$·6 H$_2$O with PP-COF-1, PP-COF-2, and PP-COF-3 were added to C$_2$H$_5$OH and refluxed for 4 h under an argon

atmosphere [45]. After the reaction, the mixture was washed with water and ethanol to remove any unbound NiCl$_2$·6 H$_2$O, and then vacuum dried at 60 °C to obtain Ni SAS-PP-COFs (noted as Ni SAS-PP-COF-1, Ni SAS-PP-COF-2, and Ni SAS-PP-COF-3, respectively).

3. Result and discussion

3.1. Synthesis and characterizations of COFs

Three PP-COFs were synthesized using the diamine of the bidentate ligand as the amine monomer of imine-based COF. Especially, PP-COFs were prepared through the polycondensation of 2,6-pyridinedicarboxaldehyde-bis-(p-aminophenylimine) (PP) with the tunable building units of 1,3,5-benzenetricarboxaldehyde, 1,3,5-tris(4-formylphenyl)benzene, and 4,4',4''-(1,3,5-triazine-2,4,6-triyl)tris[benzaldehyde], as shown in Fig. 1. Subsequently, nickel salts were added under mild conditions to anchor isolated nickel atoms at PP-COF-1, PP-COF-2, and PP-COF-3, respectively. In order to investigate the crystallinity and phase properties of these materials, powder X-ray diffraction (PXRD) was performed. To obtain accurate crystallographic data for the PP-COF, stacking structure simulations were carried out for both AA and AB modes, as
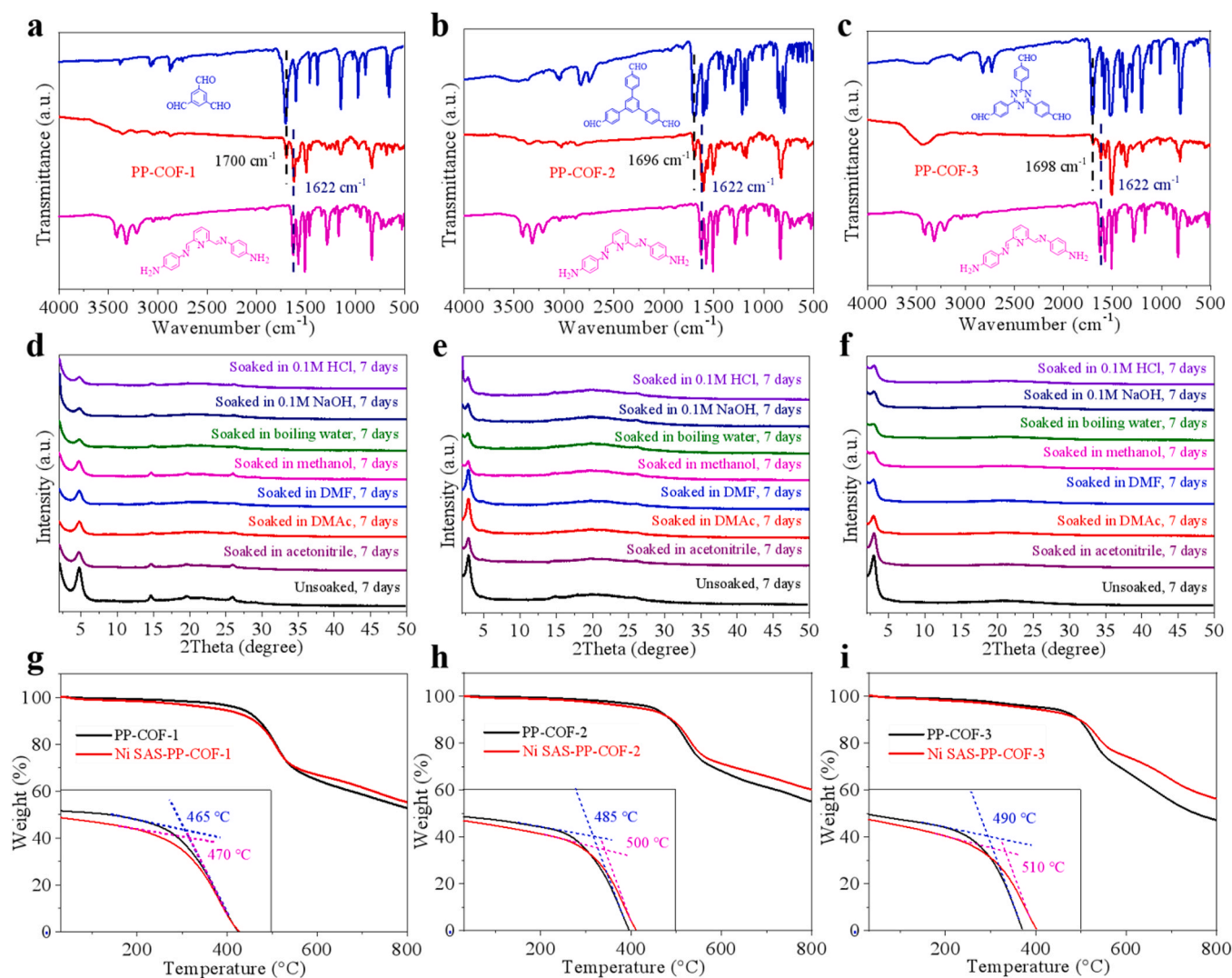
Fig. 3. FT-IR analyses of (a) PP-COF-1, (b) PP-COF-2 and (c) PP-COF-3 in comparison with the corresponding aldehyde and amine. The chemical stability of (d) PP-COF-1, (e) PP-COF-2 and (f) PP-COF-3 in 0.1 M HCl (aq), 0.1 M NaOH (aq), boiling water, methanol, dimethylformamide (DMF), dimethylacetamide (DMAc) and acetonitrile. The thermogravimetric test of (g) PP-COF-1 and Ni SAS-PP-COF-1, (h) PP-COF-2 and Ni SAS-PP-COF-2, (i) PP-COF-3 and Ni SAS-PP-COF-3.

shown in Fig. 2a-c, Figs. S3–5 and Tabs. S1–3. After geometric energy minimization, it was found that the experimental results were more consistent with the simulation results of the AA model, as shown in Fig. S6. The unit cell parameters for PP-COF-1, PP-COF-2, and PP-COF-3 were determined using the AA stacking mode, which yielded values of $a = 38.72$ Å, $b = 38.13$ Å, $c = 3.52$ Å, $\alpha = \beta = 90°$, and $\gamma = 120°$ for PP-COF-1; $a = 50.99$ Å, $b = 50.99$ Å, $c = 3.52$ Å, $\alpha = \beta = 90°$, and $\gamma = 120°$ for PP-COF-2; and $a = 50.81$ Å, $b = 50.81$ Å, $c = 3.52$ Å, $\alpha = \beta = 90°$, and $\gamma = 120°$ for PP-COF-3. The PXRD patterns of PP-COF-1, PP-COF-2, and PP-COF-3 showed the most prominent peak at 4.64°, 3.40°, and 3.40°, respectively, which can be attributed to the (110) crystal plane of the P1 space group, as shown in Fig. 2d-f. Furthermore, due to the π–π interaction in PP-COFs, the peak at 25.6 can be assigned to the (001) plane.

To refine the lattice modeling, Pawley refinement of PP-COF-1, PP-COF-2, and PP-COF-3 was performed using Materials Studio, version 7.0. PP-COF-1 was assigned to the space group P1, with parameters of $a = 38.70$ Å, $b = 38.10$ Å, $c = 3.52$ Å, $\alpha = \beta = 90°$, and $\gamma = 120°$ ($R_p = 2.22\%$ and $R_{wp} = 2.79\%$). The space groups P1 were suitable for PP-COF-2 and PP-COF-3 as well, but the parameters were marginally different ($a = 50.94$ Å, $b = 50.99$ Å, and $c = 3.52$ Å, $\alpha = \beta = 90°$, and $\gamma = 120°$ with $R_p = 4.41\%$ and $R_{wp} = 5.42\%$; $a = 50.83$ Å, $b = 50.63$ Å, and $c = 3.51$ Å, $\alpha = \beta = 90°$, and $\gamma = 120°$ with $R_p = 1.83\%$ and $R_{wp} = 2.73\%$). Lastly,

after the delocalized nickel atoms were anchored on PP-COFs, PXRD spectra of Ni SAS-PP-COFs were almost consistent with the original PP-COFs (Fig. S7), indicating that there is no obvious change in the crystal structure of PP-COFs and Ni SAS-PP-COFs.

PP-COFs were characterized using ^{13}C solid-state cross-polarization magic-angle-spinning nuclear magnetic resonance (^{13}C CP/MAS NMR) (Fig. 2g-i). For PP-COF-1 and PP-COF-2, the peaks at 148, 136–141, and 120–127 ppm were attributed to the phenyl carbon signal. The peaks at 154 and 156 ppm were assigned to the imine carbon signal. The peak at 117 ppm belonged to the terminal monomer carbon signal [57]. For PP-COF-3, the carbon signals of phenyl appeared at 146, 137, and 117–129 ppm. The carbon signal of imine showed at 154 ppm. The terminal carbon signal was observed at 107 ppm. In the Fourier-transform infrared (FT-IR) spectra of PP-COFs, the 1696–1700 cm^{-1} band corresponds to the unreacted terminal aldehyde. A stretching band at 1622 cm^{-1} confirms the formation of imine bonds (Fig. 3a-c) [58]. Compared to the aldehyde and amine monomers, the stretching bands of the aldehyde (approximately 1700 cm^{-1}) and amine (3300–3500 cm^{-1}) in PP-COFs are noticeably weakened. There is no significant difference in the FT-IR spectra of between PP-COFs and Ni SAS-PP-COFs (Figs. S8a-c). The porous properties of PP-COFs and Ni SAS-PP-COFs were analysed by nitrogen adsorption analysis at 77 K
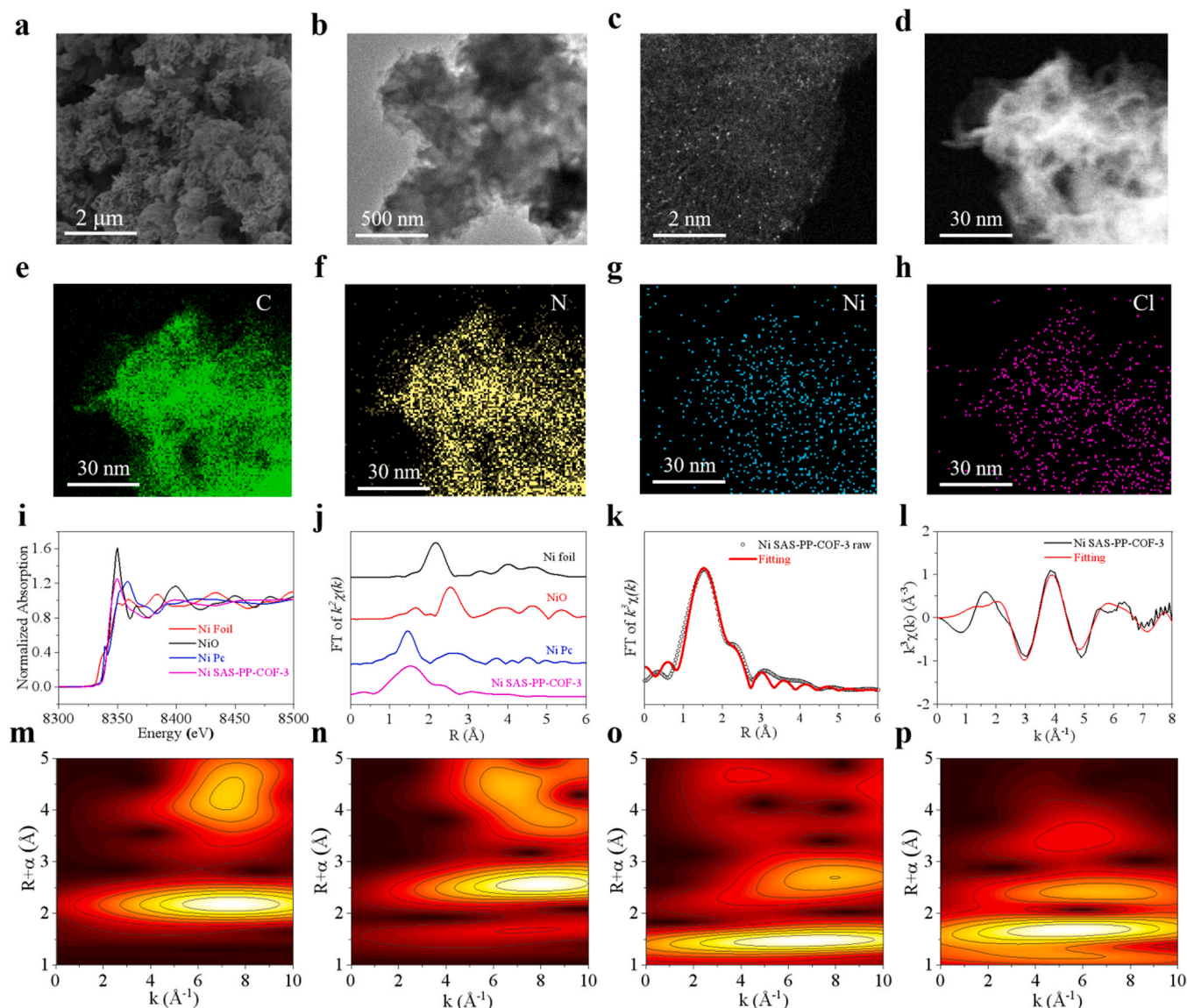
Fig. 4.. (a) SEM image and (b) TEM image of Ni SAS-PP-COF-3. (c) Z-contrast HAADF-STEM image of Ni SAS-PP-COF-3. (d-h) TEM image and element mapping of Ni SAS-PP-COF-3. (i, j) Normalized XANES and Fourier-transformed (FT) EXAFS spectra at the Ni K-edge. (k, l) The EXAFS fitting curves of Ni SAS-PP-COF-3 in R space and k space. (m-p) The WT-EXAFS of Ni foil, NiO, NiPc, and Ni SAS-PP-COF-3, respectively.

(Figs. S9-10). The Brunauer-Emmett-Teller (BET) specific surface areas of PP-COF-1, Ni SAS-PP-COF-1, PP-COF-2, Ni SAS-PP-COF-2, PP-COF-3, and Ni SAS-PP-COF-3 are 152, 55, 225, 71, 220, and 90 m^2 g^{-1}, respectively. The pore size of PP-COF-1, PP-COF-2, and PP-COF-3 measured experimentally is 1.36, 2.16, and 2.16 nm, respectively, which is consistent with the results calculated based on AA stacking. The specific surface area of Ni SAS-PP-COFs is lower than that of PP-COFs due to the chelation of Ni [59]. It can be seen from SEM and TEM that PP-COFs are not only isolated nanospheres but also have open stacks of nanosheets, which means that they have few internal pores. Therefore, the low contribution of internal pores to surface area results in low porosity. The chemical stability of PP-COFs after 7 days of treatment in 0.1 M HCl (aq), 0.1 M NaOH (aq), boiling water, methanol, dimethylformamide (DMF), dimethylacetamide (DMAc), and acetonitrile was verified by PXRD (Fig. 3d-f). PP-COFs maintain good crystallinity in boiling water, methanol, DMF, DMAc, and acetonitrile, but their crystallinity slightly decreases in 0.1 M HCl (aq) and 0.1 M NaOH (aq). The decrease in crystallinity can be attributed to the easy hydrolysis of imine bonds under acidic or alkaline conditions. Thermogravimetric analysis (TGA) shows that the weight of PP-COFs and Ni SAS-PP-COFs did not

change significantly when the temperature reached 460 °C in a nitrogen atmosphere, indicating that both PP-COFs and Ni SAS-PP-COFs have excellent thermal stability (Fig. 3g-i). The slight decrease in quality during the initial stages may be due to residual moisture and minimal unpolymerized monomer volatilization. As the temperature increases, the COF structure is destroyed and gradually pyrolyzed. The results of the elemental analysis indicate that the elemental contents of PP-COF-1, PP-COF-2, and PP-COF-3 are as follows: C: 74.35%, N: 16.86%, and H: 4.72% for PP-COF-1; C: 79.38%, N: 12.13%, and H: 4.89% for PP-COF-2; and C: 74.69%, N: 17.14%, and H: 4.38% for PP-COF-3. These values are consistent with the corresponding theoretical data for each material, which are C: 77.50%, N: 18.08%, and H: 4.42% for PP-COF-1; C: 82.35%, N: 12.98%, and H: 4.67% for PP-COF-2; and C: 77.62%, N: 18.10%, and H: 4.28% for PP-COF-3 (Tab. S4).

The structure of PP-COFs and Ni SAS-PP-COFs was characterized through various techniques including scanning electron microscopy (SEM), transmission electron microscopy (TEM), and X-ray photoelectron spectroscopy (XPS). The nanoflower morphology of both PP-COFs and Ni SAS-PP-COFs was confirmed through SEM and high-resolution TEM, as depicted in Fig. 4a,b and Figs. S11-12. The EDX mapping
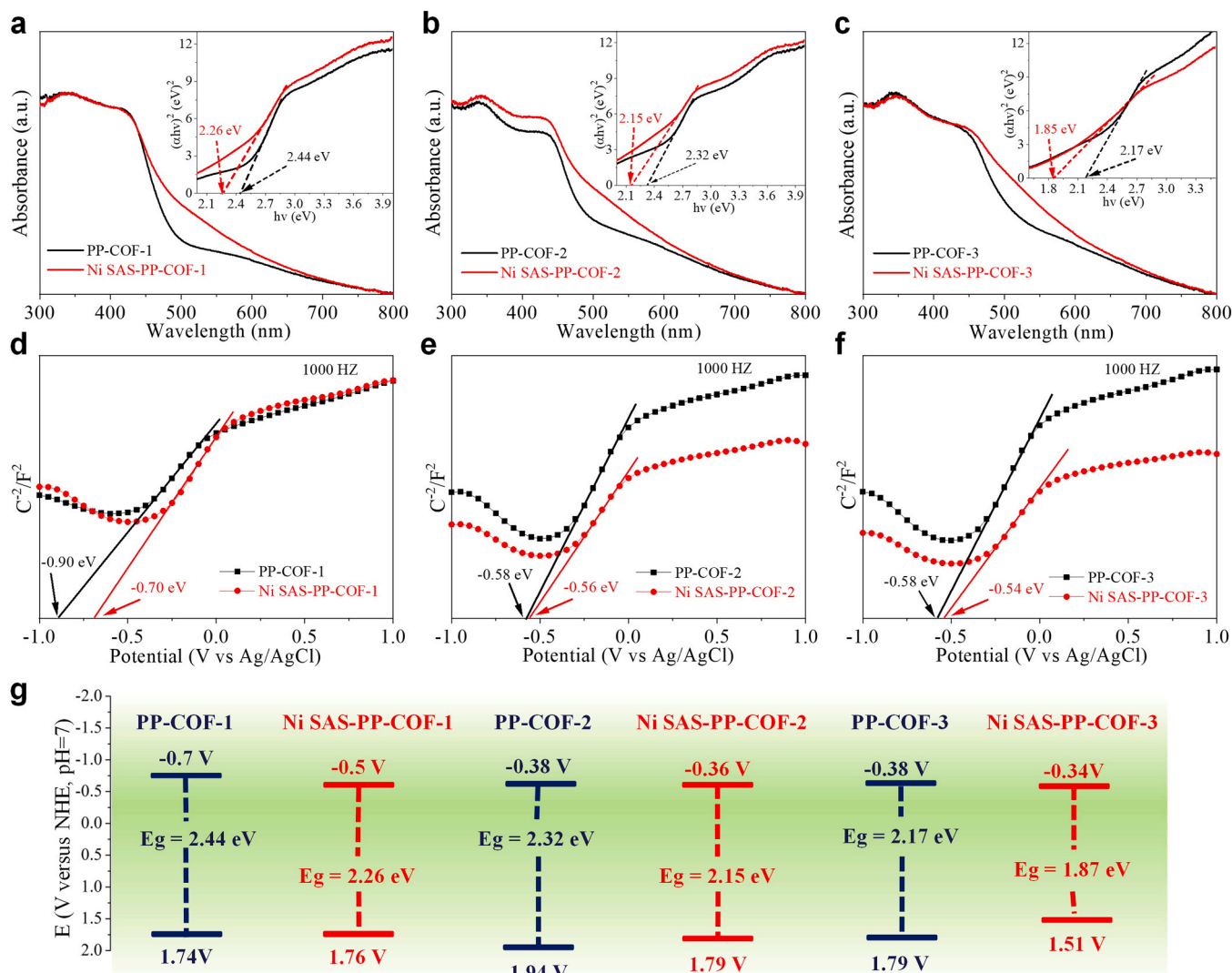
Fig. 5. (a-c) UV/Vis DRS and Band gap determined from the Kubelka–Munk-transformed reflectance spectra of PP-COF-1 and Ni SAS-PP-COF-1, PP-COF-2 and Ni SAS-PP-COF-2, PP-COF-3 and Ni SAS-PP-COF-3. (d-f) Mott-Schottky plot for PP-COF-1 and Ni SAS-PP-COF-1, PP-COF-2 and Ni SAS-PP-COF-2, PP-COF-3 and Ni SAS-PP-COF-3. (g) Band positions of PP-COF-1, PP-COF-2, PP-COF-3, Ni SAS-PP-COF-1, Ni SAS-PP-COF-2 and Ni SAS-PP-COF-3.

images of high-resolution TEM revealed the even distribution of C, N, and C, N, Ni, Cl in the skeleton of PP-COFs and Ni SAS-PP-COFs, respectively (Figs. S13-16). These findings are consistent with the results of the XPS survey spectrum (Figs. S17a-f). The Ni 2p band binding energies at 855.8 and 873.3 eV were observed in Ni SAS-PP-COFs, corresponding to Ni $2p_{3/2}$ and Ni $2p_{1/2}$ of Ni(II) ions, respectively (Figs. S17g-i) [35,48]. High-angle annular dark-field scanning transmission electron microscopy (HAADF-STEM) with aberration correction was employed to confirm the presence of Ni single atoms in Ni SAS-PP-COF-3. The atomically dispersed Ni in Ni SAS-PP-COF-3 was depicted as bright spots in the Z-contrast HAADF-STEM image (Fig. 4c). The EDX mapping images demonstrated a uniform distribution of four elements in Ni SAS-PP-COF-3 (Fig. 4d-h). The Ni content (1.20 wt%) in Ni SAS-PP-COF-3 was determined using inductively coupled plasma mass spectrometry (ICP-MS). The coordination environment of a single Ni site in Ni SAS-PP-COF-3 was analyzed through X-ray absorption near-edge structure (XANES) and extended X-ray absorption fine structure (EXAFS). The Ni K-edge XANES spectrum of Ni SAS-PP-COF-3 was shown in Fig. 4i along with Ni foil, NiO, and NiPc as references. The XANES spectra of Ni SAS-PP-COF-3 were similar to that of nickel oxide and NiPc, indicating that nickel exists in the form of divalent nickel. The Fourier transform EXAFS spectra of Ni SAS-PP-COF-3 from Fig. 4j

displayed a main peak at 1.52 Å, consistent with the first coordination shell of Ni–N. Additionally, no Ni–Ni peak was observed at 2.17 Å, indicating that the Ni site in Ni SAS-PP-COF-3 was isolated. The wavelet transform (WT) in Fig. 4m-p demonstrated that the maximum WT of Ni SAS-PP-COF-3 was 5.43 Å^{-1}, close to that of NiPc. Furthermore, the second coordination environment Ni–N–C was also found to be close to NiPc. Quantitative EXAFS analysis, as shown in Fig. 4k,l and Tab. S5, revealed that the Ni atom was bonded to two N atoms and two Cl atoms with an atomic distance of 1.99 Å (Ni–N) and 2.41 Å (Ni–Cl) in Ni SAS-PP-COF-3 [50,60]. Overall, the above results provide strong evidence for the presence of isolated Ni atoms in Ni SAS-PP-COF-3.

3.2. Band gap analysis

UV–visible diffuse reflectance spectroscopy (UV-Vis DRS) and Mott-Schottky (MS) on PP-COFs and Ni SAS-PP-COFs were conducted to investigate the optical property. UV-Vis DRS results depicted in Fig. 5a-c show that the optical band gaps of PP-COF-1, PP-COF-2, PP-COF-3, Ni SAS-PP-COF-1, Ni SAS-PP-COF-2, and Ni SAS-PP-COF-3 have been calculated to be 2.44, 2.32, 2.17, 2.26, 2.15 and 1.85 eV, respectively, using the Kubelka-Munk theory [61,62]. Moreover, the Mott-Schottky test was used to analyze the flat band potentials of PP-COF and Ni
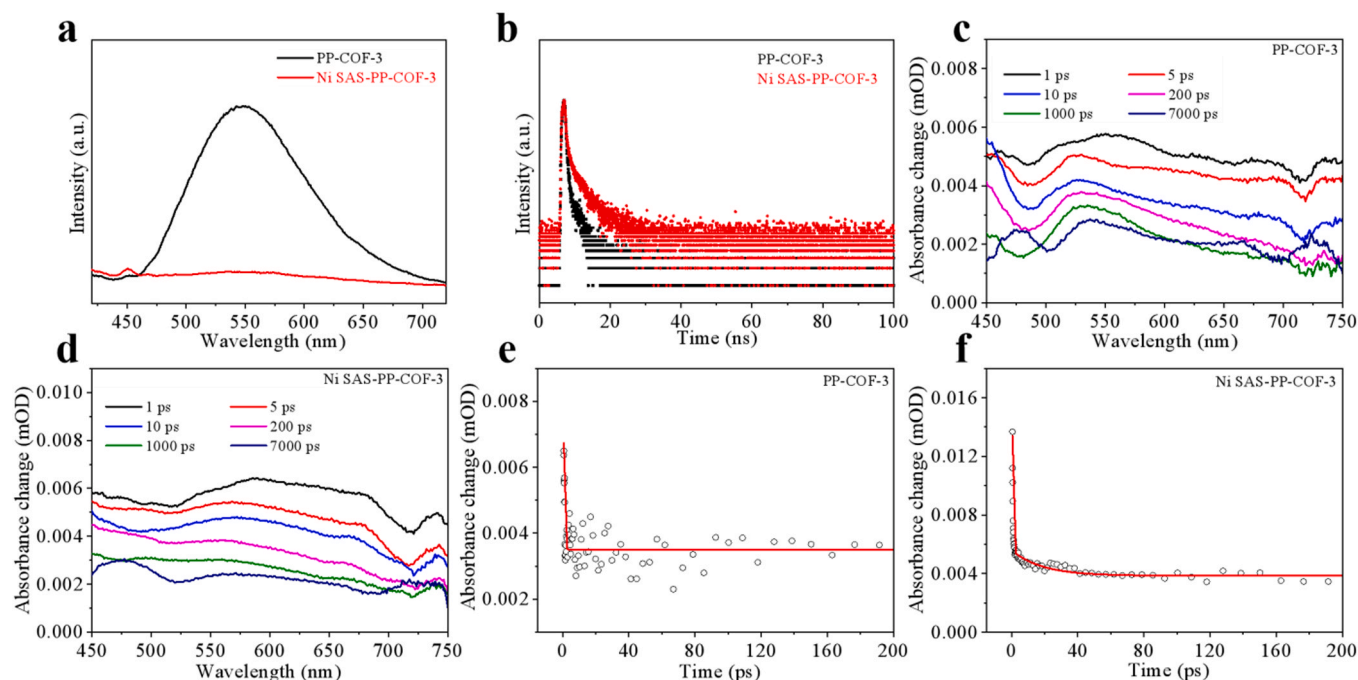
Fig. 6. (a) PL spectra of of PP-COF-3 and Ni SAS-PP-COF-3. (b) Transient state photoluminescence spectra of PP-COF-3 and Ni SAS-PP-COF-3. Transient fs-TA spectra of (c) PP-COF-3 and (d) Ni SAS-PP-COF-3 under various probe delays. TA kinetics plots and typical fitting curves of (e) PP-COF-3 and (f) Ni SAS-PP-COF-3 probed at 550 nm probe wavelength.

SAS-PP-COF at 1000 Hz, as shown in Fig. 5d-f. The positive slope of the curves indicates that both PP-COFs and Ni SAS-PP-COFs are n-type semiconductors [63–65]. Combining the flat-band potential and the band gap, the band structures of PP-COF and Ni SAS-PP-COF were established, as shown in Fig. 5 g. To confirm that the photocatalyst can reduce the nickel anchored on Ni SAS-PP-COF-3, cyclic voltammetry was performed, as shown in Fig. S18. Compared with PP-COF-3, Ni SAS-PP-COF-3 exhibited two noticeable reduction peaks at − 0.38 V (R₁) and − 1.23 V (R₂), versus Ag/AgCl electrode (−0.18 V (R₁) and − 1.03 V (R₂), versus NHE, pH = 7), representing the reduction of Ni (II)/Ni(I) and Ni(II)/Ni(0), respectively [66,67]. Therefore, Ni SAS-PP-COFs can reduce the Ni(II) anchored on it to Ni(I) but not further

to Ni(0) [45,48,56].

3.3. Spectral characterization

Steady-state photoluminescence (PL) and time-resolved transient photoluminescence (TRPL) spectra were conducted to investigate photogenerated carrier separation and photogenerated electron-hole lifetime. As shown in Fig. 6a and Figs. S19a,b, the PL intensity of Ni SAS-PP-COFs decreased sharply compared to PP-COFs, demonstrating that anchoring a single nickel atom on PP-COFs can effectively inhibit electron-hole recombination. Additionally, the TRPL results further indicated that Ni SAS-PP-COFs have a longer carrier lifetime than PP-

Table 1
Optimization of the reaction conditions.

Entry	Deviation	Yield [%][b]
1	Standard conditions[a]	99 (96)[c]
2	No light (dark)	No product
3	No Ni SAS-PP-COF-3	No product
4	No base	63
5	PP-COF-3 instead of Ni SAS-PP-COF-3	No product
6	PP-COF-3 + NiCl₂·6 H₂O instead of Ni SAS-PP-COF-3	32
7	Ni SAS-PP-COF-1 instead of Ni SAS-PP-COF-3	74
8	Ni SAS-PP-COF-2 instead of Ni SAS-PP-COF-3	88

[a]Standard conditions: Ar atmosphere, room temperature, 15 h, 4-bromobenzotrifluoride (1.0 mmol, 1.0 equiv.), Ni SAS-PP-COF-3 (10 mg, 1 mg mL⁻¹), morpholine (2.0 mmol, 2 equiv.), DABCO (1.5 mmol, 1.5 equiv.) in DMA (10.0 mL). [b]Yields determined by ¹H NMR using 1,3-benzodioxole as an internal standard. [c]Isolated yield.
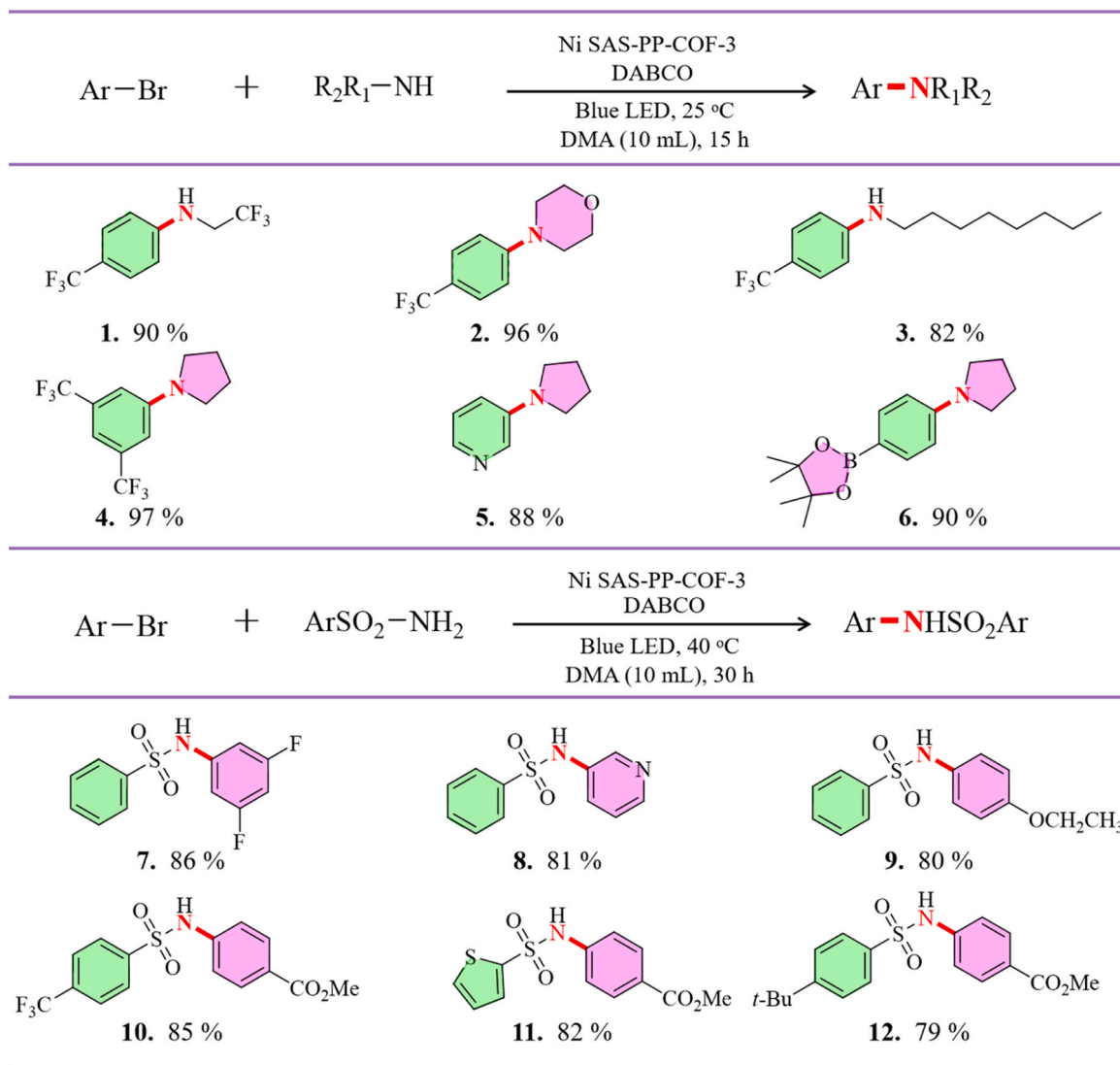
Fig. 7. Ar atmosphere, DABCO (1.5 mmol, 1.5 equiv.), Ni SAS-PP-COF-3 (1 mg mL^{-1}), 450 nm LED, aryl bromides (1.0 mmol, 1.0 equiv.), amines (2.0 mmol, 2.0 equiv.), DMA (10 mL), isolated yields.

COFs (As shown in Fig. 6b, Figs. S19c,d and Tab. S6). Among Ni SAS-PP-COFs, Ni SAS-PP-COF-3 exhibited the longest lifetime, approximately 1.6 times that of PP-COF-3. To further investigate the role of a single nickel atom in PP-COF, transient absorption (TA) spectroscopy was conducted on PP-COF-3 and Ni SAS-PP-COF-3. Positive characteristics of PP-COF-3 and Ni SAS-PP-COF-3 were observed at 550 nm in TA spectra. This can be attributed to the absorption of intramolecular charge transfer in the excited state (Fig. 6c,d). The TA dynamics of PP-COF-3 and Ni SAS-PP-COF-3 at 550 nm probe wavelengths are presented in Fig. 6e,f, respectively. The kinetic details fitted at different wavelengths are given in Tab. S7. Importantly, Ni SAS-PP-COF-3 (τ = 26.47 ps) displayed a longer lifetime than PP-COF-3 (τ = 11.53 ps), indicating the migration of electrons from PP-COF-3 to a single Ni site.

3.4. Optimization of conditions and expansion of substrates

Based on the results presented above, Ni SAS-PP-COFs present great potential as a dual catalyst for C–N cross-coupling reactions. To achieve optimal coupling yields, reaction conditions were optimized using 4-bromobenzotrifluoride and morpholine as model substrates (Table 1). The optimized reaction mixture was prepared by sequentially adding Ni SAS-PP-COF, 1,4-diazabicyclo[2.2.2]octane, 4-bromobenzotrifluoride

and morpholine to N,N-dimethylacetamide in a reactor. When Ni SAS-PP-COF-3 was used as the photocatalyst and the reaction was subjected to blue LED irradiation, the coupling product 4-(4-(trifluoromethyl)phenyl)morpholine was obtained in high yield (99%, as determined by ^{1}H NMR) after 15 h (Table 1, entry 1). No coupling product was observed in the absence of light or photocatalyst (Table 1, entries 2–3). Furthermore, the yield of the target product decreased when the base was not included (Table 1, entry 4). The necessity of Ni species was confirmed by the lack of coupling product formation when Ni SAS-PP-COF-3 was replaced with PP-COF-3 (Table 1, entry 5). When a mixture of nickel salt and PP-COF-3 was used instead of Ni SAS-PP-COF-3, the yield of the coupling product was only 32% (Table 1, entry 6). Finally, when Ni SAS-PP-COF-1 and Ni SAS-PP-COF-2 were used in place of Ni SAS-PP-COF-3, the coupling yields were 74% and 88%, respectively (Table 1, entries 7–8). The performance was compared with some inorganic and homogeneous catalysts, and a showed the highest performance (Tab. S8). Building upon the optimization of the model reaction, the substrate scope of the C–N cross-coupling reaction was expanded. Specifically, 4-bromobenzotrifluoride was used as the aryl bromide model substrate to react with electron-withdrawing, neutral, and electron-rich amine substrates, respectively, and pyrrolidine was used as a model substrate for amine compounds to couple with aryl
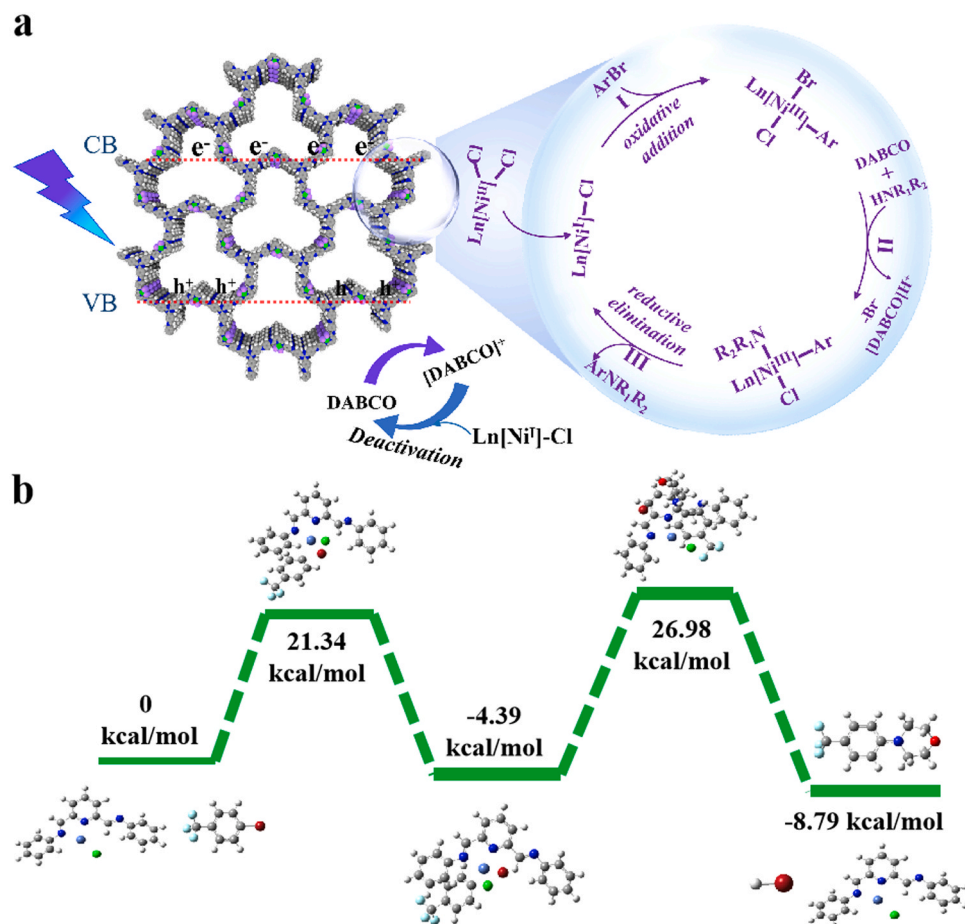
Fig. 8. (a) Proposed catalytic cycle for the C–N coupling reactions catalyzed by Ni SAS-PP-COF. (b) Calculated Gibbs free energy profile of Ni SAS-PP-COF catalyzed amination reaction.

bromides with different electron groups. The substrate ratio of the model reaction was optimized, and subsequent substrate expansion was performed according to this optimized ratio (Tab. S9). The results show that aryl bromides can be successfully coupled with alkylamines in excellent yields (Fig. 7, 1–6, 82–97%). In addition, benzenesulfonamide was used as an amine model substrate to react with aryl bromides with different electronic properties, and methyl 4-bromobenzoate was used as an aryl bromide model substrate to react with sulfonamides with different electronic properties. In both cases, coupling products were obtained in excellent yields (Fig. 7, 7-12, 79–86%).

3.5. Mechanism analysis

In order to explore the influence of various additives on the luminescence quenching of PP-COFs, the luminescence quenching rates of different sacrificial agent systems were compared for PP-COF-3. As shown in Fig. S20, with low Ni loading of PP-COF-3 as well as a slight increase in loading amount, the luminescence intensity in PP-COF-3 decreases sharply. Only a slight decrease in intensity was observed when 1a, 2a and DABCO were added to PP-COF-3, respectively. The luminous intensity curves exhibit a commendable concordance with the Stern-Volmer equation, providing Stern-Volmer (K_{SV}) constant values of 15.64, 0.01, 0.02, and 0.09 for Ni SAS-PP-COF-3, 1a, 2a, and DABCO, respectively. Through a comparative analysis of quenching constants, it was conclusively established that the nickel atoms anchored to the COF matrix play a pivotal role in the quenching of the photocatalyst. This observation suggests that an electron transfer pathway from PP-COF-3 to Ni is operative. The transient photocurrents of PP-COFs and Ni SAS-PP-COFs electrodes were measured, revealing that the Ni SAS-PP-COFs

photoelectrode had a higher photocurrent signal compared to PP-COFs, indicating an improvement in the separation and transfer of electrons and holes (Figs. S21a-c). Similarly, electrochemical impedance spectroscopy (EIS) tests of PP-COFs and Ni SAS-PP-COFs also yielded comparable outcomes. Figs. S21d-f shows that Ni SAS-PP-COFs had a smaller arc radius than PP-COFs, indicating lower interface charge transfer resistance.

Compared to homogeneous catalysts, heterogeneous catalysts offer the prominent advantage of being separated and recovered at a lower cost. By centrifuging the previous reaction solution, the catalyst for the next cycle reaction can be obtained. Remarkably, even after six catalytic cycles, the reaction can still proceed with an excellent yield (Fig. S22). We conducted intermittent switching light performance tests and demonstrated that light plays a crucial role in the catalytic system (Fig. S23). The catalysts were characterized by XRD, BET, SEM, IR, and XPS after the reaction. The consistent XRD before and after the reaction indicates that the crystal structure of these materials remains unchanged (Fig. S24). The test results of BET show that the specific surface area is well maintained after six catalytic cycles (Fig. S25). Moreover, the SEM after the reaction still retained the original rough morphology, as shown in Fig. S26. The IR and XPS spectra after the reaction were also similar to those before the reaction, indicating excellent stability of the material.

Combining our experimental results with previous literature reports, we propose a catalytic cycle for the coupling reaction, as illustrated in Fig. 8a. Ni SAS-PP-COFs generate photogenerated electron-hole pairs upon visible light excitation. Analysis of cyclic voltammetry indicates that the photogenerated electrons can reduce Ni(II) to Ni(I) but not further to Ni(0). Once Ni(I) is formed, it undergoes oxidative addition with aryl bromides to form Ni(III) complexes, followed by ligand

exchange and reduction elimination to form C–N coupling products. Reduction of the Ni(III) intermediate by accumulated electrons and reoxidation of Ni(I) by the DABCO radical cation can close the cycle. To verify the feasibility of this reaction mechanism, DFT calculations of the model reaction were performed using the model of Ni SAS-PP-COFs, as shown in Fig. 8b. The reaction begins with the oxidative addition of aryl bromide to Ni(I), with a reaction energy barrier of 21.34 kcal mol^{-1}. The bromine atom on the resulting pentacoordinate Ni(III) species is then exchanged for morpholine. Finally, the coupling product could be obtained through reductive elimination.

4. Conclusion

In summary, we reported three novel imine-based bi-coordinated two-dimensional covalent organic frameworks with atomically dispersed Ni active sites. The isolated nickel catalytic sites and coordination environment were convinced by distortion-corrected high-angle annular dark-field scanning transmission electron microscopy and extended X-ray absorption fine structure. In comparison to Ni SAS-PP-COF-1 and Ni SAS-PP-COF-2, this state-of-the-art Ni SAS-PP-COF-3 catalyst exhibits significant functional group tolerance and high yield (79–97%) for photo/Ni dual-catalyzed C–N cross-coupling between aryl bromides and alkyl/sulfo amines due to the increased charge separation, abundant active sites and high charge carrier separation efficiency. This work not only expands the members of COF-based heterogeneous catalysts, but also provides in-depth insights into the rational design of photoredox/transition catalytic systems.

CRediT authorship contribution statement

Sun Licheng: Writing – review & editing. **Li Zhuwei:** Investigation, Methodology, Writing – original draft, Writing – review & editing. **Hou Jungang:** Project administration, Writing – review & editing. **Cheng Huijie:** Methodology. **Li Yaning:** Methodology. **Jiao Yuye:** Methodology. **Song Yurou:** Methodology. **Gao Junfeng:** Methodology. **Shi Shaobo:** Methodology.

Declaration of Competing Interest

All authors declare that they have no known competing financial interests or personal relationships that could have appeared to influence the work reported in this paper.

Data availability

Data will be made available on request.

Acknowledgements

Appendix A. Supporting information

Supplementary data associated with this article can be found in the online version at doi:10.1016/j.apcatb.2024.123698.

References

[1] A.P. Cote, A.I. Benin, N.W. Ockwig, M. O'Keeffe, A.J. Matzger, O.M. Yaghi, Porous, crystalline, covalent organic frameworks, Science 310 (2005) 1166–1170.

[2] H.M. El-Kaderi, J.R. Hunt, J.L. Mendoza-Cortes, A.P. Cote, R.E. Taylor, M. O'Keeffe, O.M. Yaghi, Designed synthesis of 3D covalent organic frameworks, Science 316 (2007) 268–272.

[3] P.J. Waller, F. Gandara, O.M. Yaghi, Chemistry of covalent organic frameworks, Acc. Chem. Res. 48 (2015) 3053–3063.

[4] C.S. Diercks, O.M. Yaghi, The atom, the molecule, and the covalent organic framework, Science 355 (2007) 268–272.

[5] S. Canossa, Z. Ji, C. Gropp, Z. Rong, E. Ploetz, S. Wuttke, O.M. Yaghi, System of sequences in multivariate reticular structures, Nat. Rev. Mater. (2022), https://doi.org/10.1038/s41578-022-00482-5.

[6] C. Gropp, T. Ma, N. Hanikel, O.M. Yaghi, Design of higher valency in covalent organic frameworks, Science 370 (2020) eabd6406.

[7] K. Geng, T. He, R. Liu, S. Dalapati, K.T. Tan, Z. Li, S. Tao, Y. Gong, Q. Jiang, D. L. Jiang, Covalent organic frameworks: design, synthesis, and functions, Chem. Rev. 120 (2020) 8814–8933.

[8] M. Liu, Y., J. Chen, X. Huang, L.Z. Dong, M. Lu, C. Guo, D. Yuan, Y. Chen, G. Xu, S. L. Li, Y.Q. Lan, Porphyrin-based COF 2D materials: variable modification of sensing performances by post-metallization, Angew. Chem. Int. Ed. 61 (2022) e202115308.

[9] S. Wang, X.X. Li, L. Da, Y. Wang, Z. Xiang, W. Wang, Y.B. Zhang, D.P. Cao, A three-dimensional sp2 carbon-conjugated covalent organic framework, J. Am. Chem. Soc. 143 (2021) 15562–15566.

[10] H. Fan, M. Peng, I. Strauss, A. Mundstock, H. Meng, J. Caro, High-flux vertically aligned 2D covalent organic framework membrane with enhanced hydrogen separation, J. Am. Chem. Soc. 142 (2020) 6872–6877.

[11] F. Jin, E. Lin, T. Wang, S. Geng, L. Hao, Q. Zhu, Z. Wang, Y. Chen, P. Cheng, Z. J. Zhang, Rationally fabricating three-dimensional covalent organic frameworks for propyne/propylene separation, J. Am. Chem. Soc. 144 (2022) 23081–23088.

[12] J. Li, Z. Cheng, Z. Wang, J. Dong, H. Jiang, W. Wang, X. Zou, G.S. Zhu, Ultramicroporous covalent organic framework nanosheets with functionality pair for membrane C$_2$H$_2$/C$_2$H$_4$ separation, Angew. Chem. Int. Ed. 62 (2023) e202216675.

[13] H. Fan, A. Mundstock, A. Feldhoff, A. Knebel, J. Gu, H. Meng, J. Caro, Covalent organic framework−covalent organic framework bilayer membranes for highly selective gas separation, J. Am. Chem. Soc. 140 (2018) 10094–10098.

[14] L. Yao, A.R. Camargo, M. Xia, D. Mücke, R. Guntermann, Y. Liu, L. Grunenberg, A. J. Solano, S.T. Emmerling, V. Duppel, K. Sivula, T. Bein, H. Qi, U. Kaiser, M. Grätzel, B.V. Lotsch, Covalent organic framework nanoplates enable solution-processed crystalline nanofilms for photoelectrochemical hydrogen evolution, J. Am. Chem. Soc. 144 (2022) 10291–10300.

[15] Y. Xiong, Q. Liao, Z. Huang, X. Huang, C. Ke, H. Zhu, C. Dong, H. Wang, K. Xi, P. Zhan, F. Xu, Y. Lu, Ultrahigh responsivity photodetectors of 2D covalent organic frameworks integrated on grapheme, Adv. Mater. 32 (2020) 1907242.

[16] T. Sick, A.G. Hufnagel, J. Kampmann, I. Kondofersky, M. Calik, J.M. Rotter, A. Evans, M. Döblinger, S. Herbert, K. Peters, D. Böhm, P. Knochel, D.D. Medina, D. F. Rohlfing, T. Bein, Oriented films of conjugated 2D covalent organic frameworks as photocathodes for water splitting, J. Am. Chem. Soc. 140 (2018) 2085–2092.

[17] Y. Xu, P. Cai, K. Chen, Q. Chen, Z. Wen, L. Chen, Hybrid acid/alkali all covalent organic frameworks battery, Angew. Chem. Int. Ed. (2023) e202215584.

[18] S. Haldar, M. Wang, P. Bhauriyal, A. Hazra, A.H. Khan, V. Bon, M.A. Isaacs, A. De, L. Shupletsov, T. Boenke, J. Grothe, T. Heine, E. Brunner, X. Feng, R. Dong, A. Schneemann, S. Kaskel, Porous dithiine-linked covalent organic framework as a dynamic platform for covalent polysulfide anchoring in lithium−sulfur battery cathodes, J. Am. Chem. Soc. 144 (2022) 9101–9112.

[19] Y. Lin, H. Cui, C. Liu, R. Li, S. Wang, G. Qu, Z. Wei, Y. Yang, Y. Wang, Z. Tang, H. Li, H. Zhang, C.Y. Zhi, H.M. Lv, A covalent organic framework as a long-life and high-rate anode suitable for both aqueous acidic and alkaline batteries, Angew. Chem. Int. Ed. (2023) e202218745.

[20] Y. Yang, P. Zhang, L. Hao, P. Cheng, Y. Chen, Z.J. Zhang, Grotthuss proton-conductive covalent organic frameworks for efficient proton pseudocapacitors, Angew. Chem. Int. Ed. 60 (2021) 21838–21845.

[21] B. Shi, X. Pang, B. Lyu, H. Wu, J. Shen, J. Guan, X. Wang, C. Fan, L. Cao, T. Zhu, Y. Kong, Y. Liu, Z.Y. Jiang, Spacer-engineered ionic channels in covalent organic framework membranes toward ultrafast proton transport, Adv. Mater. (2023) 2211004.

[22] X. Wu, Y. Hong, B. Xu, Y. Nishiyama, W. Jiang, J. Zhu, G. Zhang, S. Kitagawa, S. Horike, Perfluoroalkyl-functionalized covalent organic frameworks with superhydrophobicity for anhydrous proton conduction, J. Am. Chem. Soc. 142 (2020) 14357–14364.

[23] Y. Yang, X. Chu, H.Y. Zhang, R. Zhang, Y.H. Liu, F.M. Zhang, M. Lu, Z.D. Yang, Y. Q. Lan, Engineering β-ketoamine covalent organic frameworks for photocatalytic overall water splitting, Nat. Commun. 14 (2023) 593.

[24] J.N. Chang, Q. Li, J.W. Shi, M. Zhang, L. Zhang, S. Li, Y. Chen, S.L. Li, Y.Q. Lan, Oxidation-reduction molecular junction covalent organic frameworks for full reaction photosynthesis of H$_2$O$_2$, Angew. Chem. Int. Ed. (2023) e202218868.

[25] M. Lu, M. Zhang, J. Liu, T.Y. Yu, J.N. Chang, L.J. Shang, S.L. Li, Y.Q. Lan, Confining and highly dispersing single polyoxometalate clusters in covalent organic frameworks by covalent linkages for CO$_2$ photoreduction, J. Am. Chem. Soc. 144 (2022) 1861–1871.

[26] J.N. Chang, Q. Li, Y. Yan, J.W. Shi, J. Zhou, M. Lu, M. Zhang, H.M. Ding, Y. Chen, S.L. Li, Y.Q. Lan, Covalent-bonding oxidation group and titanium cluster to synthesize a porous crystalline catalyst for selective photo oxidation biomass valorization, Angew. Chem. Int. Ed. 61 (2022) e202209289.

[27] N. Li, D.H. Si, Q.J. Wu, Q. Wu, Y.B. Huang, R. Cao, Boosting electrocatalytic CO$_2$ reduction with conjugated bimetallic Co/Zn polyphthalocyanine frameworks, CCS Chem. 5 (2022) 1130–1143.

[28] S.S. Zhao, J. Liang, D.H. Si, M.J. Mao, Y.B. Huang, R. Cao, Superheterojunction covalent organic frameworks: supramolecular synergetic charge transfer for highly efficient photocatalytic CO_2 reduction, Appl. Catal. B Environ. 333 (2023) 122782..

[29] R. Xu, D.H. Si, S.S. Zhao, Q.J. Wu, X.S. Wang, T.F. Liu, H. Zhao, R. Cao, Y.B. Huang, Tandem photocatalysis of CO_2 to C_2H_4 via a synergistic rhenium-(I) bipyridine/ copper-porphyrinic triazine framework, J. Am. Chem. Soc. 145 (2023) 8261–8270.

[30] X.T. Li, J. Zou, T.H. Wang, H.C. Ma, G.J. Chen, Y.B. Dong, Construction of covalent organic frameworks via three component one-pot strecker and povarov reactions, J. Am. Chem. Soc. 142 (2020) 6521–6526.

[31] H.L. Nguyen, F. Gandara, H. Furukawa, T.L.H. Doan, K.E. Cordova, O.M. Yaghi, A titanium-organic framework as an exemplar of combining the chemistry of metal- and covalent-organic frameworks, J. Am. Chem. Soc. 138 (2016) 4330–4333.

[32] Q. Yang, M. Luo, K. Liu, H. Cao, H.J. Yan, Covalent organic frameworks for photocatalytic applications, Appl. Catal. B Environ. 276 (2020) 119174.

[33] G. Kumar, R.S. Pillai, N.H. Khan, S. N. Structural engineering in pre-functionalized, imine-based covalent organic framework via anchoring active Ru(II)-complex for visible-light triggered and aerobic cross-coupling of α-amino esters with indoles, Appl. Catal. B Environ. 292 (2021) 120149.

[34] Y. Meng, Y. Luo, J.L. Shi, H. Ding, X. Lang, W. Chen, A. Zheng, J. Sun, C. Wang, 2D and 3D porphyrinic covalent organic frameworks: the influence of dimensionality on functionality, Angew. Chem. Int. Ed. 59 (2020) 3624–3629.

[35] W. Zhong, R. Sa, L. Li, Y. He, L. Li, J. Bi, Z. Zhuang, Y. Yu, Z.G. Zou, A covalent organic framework bearing single Ni sites as a synergistic photocatalyst for selective photoreduction of CO_2 to CO, J. Am. Chem. Soc. 141 (2019) 7615–7621.

[36] A. Jati, K. Dey, M. Nurhuda, M.A. Addicoat, R. Banerjee, B. Maji, Dual metalation in a two-dimensional covalent organic framework for photocatalytic C−N cross-coupling reactions, J. Am. Chem. Soc. 144 (2022) 7822–7833.

[37] F. Li, J.L. Kan, B.J. Yao, Y.B. Dong, Synthesis of chiral covalent organic frameworks via asymmetric organocatalysis for heterogeneous asymmetric catalysis, Angew. Chem. Int. Ed. 61 (2022) e202115044.

[38] D. Li, C. Li, L. Zhang, H. Li, L. Zhu, D. Yang, Q.R. Fang, S. Qiu, X.D. Yao, Metal-free thiophene-sulfur covalent organic frameworks: precise and controllable synthesis of catalytic active sites for oxygen reduction, J. Am. Chem. Soc. 142 (2020) 8104–8108.

[39] N. Keller, D. Bessinger, S. Reuter, M. Calik, L. Ascherl, F.C. Hanusch, F. Auras, T. Bein, Oligothiophene-bridged conjugated covalent organic frameworks, J. Am. Chem. Soc. 139 (2017) 8194–8199.

[40] S. Wang, L. Da, J. Hao, J. Li, M. Wang, Y. Huang, Z. Li, Z. Liu, D.P. Cao, A fully conjugated 3D covalent organic framework exhibiting band-like transport with ultrahigh electron mobility, Angew. Chem. Int. Ed. 60 (2021) 9321–9325.

[41] L. Ran, Z. Li, B. Ran, J. Cao, Y. Zhao, T. Shao, Y. Song, M.K.H. Leung, L. Sun, J. G. Hou, Engineering single-atom active sites on covalent organic frameworks for boosting CO_2 photoreduction, J. Am. Chem. Soc. 144 (2022) 17097–17109.

[42] L. Sun, M. Lu, Z. Yang, Z. Yu, X. Su, Y.Q. Lan, L. Chen, Nickel glyoxime based metal–covalent organic frameworks for efficient photocatalytic hydrogen evolution, Angew. Chem. Int. Ed. (2022) e202204326.

[43] Y. Zhang, L. Cao, G.Y. Bai, X.W. Lan, Engineering single Cu sites into covalent organic framework for selective photocatalytic CO_2 reduction, Small (2023) 2300035.

[44] Q. Zhang, S. Gao, Y. Guo, H. Wang, J. Wei, X. Su, H. Zhang, Z. Liu, J.J. Wang, Designing covalent organic frameworks with Co-O₄ atomic sites for efficient CO_2 photoreduction, Nat. Commun. 14 (2023) 1147.

[45] W. Dong, Y. Yang, Y. Xiang, S. Wang, P. Wang, J. Hu, L. Rao, H. Chen, A highly stable all-in-one photocatalyst for aryl etherification: the NiII embedded covalent organic framework, Green Chem. 23 (2021) 5797–5805.

[46] M. Traxler, S. Gisbertz, P. Pachfule, J. Schmidt, J. Roeser, S. Reischauer, J. Rabeah, B. Pieber, A. Thomas, Acridine-functionalized covalent organic frameworks (COFs) as photocatalysts for metallaphotocatalytic C−N Cross-Coupling, Angew. Chem. Int. Ed. 61 (2022) e202117738.

[47] A. Vijeta, C. Casadevall, S. Roy, E. Reisner, Visible-light promoted C–O bond formation with an integrated carbon nitride–nickel heterogeneous photocatalyst, Angew. Chem. Int. Ed. 60 (2021) 8494–8499.

[48] H. Chen, W. Liu, A. Laemont, C. Krishnaraj, X. Feng, F. Rohman, M. Meledina, Q. Zhang, R.V. Deun, K. Leus, P.V.D. Voort, A visible-light-harvesting covalent organic framework bearing single nickel sites as a highly efficient sulfur–carbon cross-coupling dual catalyst, Angew. Chem. Int. Ed. 60 (2021) 10820–10827.

[49] Y.Y. Zhu, G. Lan, Y. Fan, S.S. Veroneau, Y. Song, D. Micheroni, W.B. Lin, Merging photoredox and organometallic catalysts in a metal–organic framework significantly boosts photocatalytic activities, Angew. Chem. Int. Ed. 130 (2018) 14286–14290.

[50] G. Lan, Y. Quan, M. Wang, G.T. Nash, E. You, Y. Song, S.S. Veroneau, X. Jiang, W. B. Lin, Metal−organic layers as multifunctional two-dimensional nanomaterials for enhanced photoredox catalysis, J. Am. Chem. Soc. 141 (2019) 15767–15772.

[51] S. Gisbertz, S. Reischauer, B. Pieber, Overcoming limitations in dual photoredox/ nickel-catalysed C−N cross-couplings due to catalyst deactivation, Nat. Catal. 3 (2020) 611–620.

[52] C. Cavedon, A. Madani, P.H. Seeberger, B. Pieber, Semiheterogeneous dual nickel/ photocatalytic (thio)etherification using carbon nitrides, Org. Lett. 21 (2019) 5331–5334.

[53] Y. Qin, B.C.M. Martindale, R. Sun, A.J. Rieth, D.G. Nocera, Solar-driven tandem photoredox nickel-catalysed cross-coupling using modified carbon nitride, Chem. Sci. 11 (2020) 7456–7461.

[54] J.A. Caputo, L.C. Frenette, N. Zhao, K.L. Sowers, T.D. Krauss, D.J. Weix, General and efficient C−C bond forming photoredox catalysis with semiconductor quantum dots, J. Am. Chem. Soc. 139 (2017) 4250–4253.

[55] X. Zhu, Y. Lin, J.S. Martin, Y. Sun, D. Zhu, Y. Yan, Lead halide perovskites for photocatalytic organic synthesis, Nat. Commun. 10 (2019) 2843.

[56] A.L. Magano, B.O. Rubio, I. Imaz, D. Maspoch, J. Alemán, R.M. Ballesté, Photoredox heterobimetallic dual catalysis using engineered covalent organic frameworks, ACS Catal. 11 (2021) 12344–12354.

[57] A.M. Kaczmarek, H.S. Jena, C. Krishnaraj, H. Rijckaert, S.K.P. Veerapandian, A. Meijerink, P.V.D. Voort, Luminescent ratiometric thermometers based on a 4f–3d grafted covalent organic framework to locally measure temperature gradients during catalytic reactions, Angew. Chem. Int. Ed. 60 (2021) 3727–3736.

[58] C. Krishnaraj, A.M. Kaczmarek, H.S. Jena, K. Leus, N. Chaoui, J. Schmidt, R. V. Deun, P.V.D. Voort, Triggering white-light emission in a 2D imine covalent organic framework through lanthanide augmentation, ACS Appl. Mater. Interfaces 11 (2019) 27343–27352.

[59] Z. Li, S. Qiu, Y. Song, S. Huang, J. Gao, L. Sun, J.G. Hou, Engineering single–atom active sites anchored covalent organic frameworks for efficient metallaphotoredox C–N cross–coupling reactions, Sci. Bull. 67 (2022) 1971–1981.

[60] Y. Quan, W. Shi, Y. Song, X. Jiang, C. Wang, W.B. Lin, Bifunctional metal−organic layer with organic dyes and iron centers for synergistic photoredox catalysis, J. Am. Chem. Soc. 143 (2021) 3075–3080.

[61] Y. Zhang, L. Ran, Y. Zhang, P. Zhai, Y. Wu, J. Gao, Z. Li, B. Zhang, C. Wang, Z. Fan, X. Zhang, J. Cao, D. Jin, L. Sun, J.G. Hou, Two-dimensional defective boron-doped niobic acid nanosheets for robust nitrogen photofixation, ACS Nano. 15 (2021) 17820–17830.

[62] Z. Li, Y. Song, T. Shao, S. Huang, L. Sun, J.G. Hou, Integrated nickel/polymer dual catalytic system for visible-light-driven sulfonamidation between aryl halides and aryl sulfonamides, Chem. Catal. 2 (2022) 3546–3558.

[63] S. Bi, C. Yang, W. Zhang, J. Xu, L. Liu, D. Wu, X. Wang, Y. Han, Q. Liang, F. Zhang, Two-dimensional semiconducting covalent organic frameworks via condensation at arylmethyl carbon atoms, Nat. Commun. 10 (2019) 2467.

[64] X. Zhang, P. Zhai, Y. Zhang, Y. Wu, C. Wang, L. Ran, J. Gao, Z. Li, B. Zhang, Z. Fan, L. Sun, J.G. Hou, Engineering single-atomic Ni-N₄-O sites on semiconductor photoanodes for high-performance photoelectrochemical water splitting, J. Am. Chem. Soc. 143 (2021) 20657–20669.

[65] Y. Song, X. Zhang, Y. Zhang, P. Zhai, Z. Li, D. Jin, J. Cao, C. Wang, B. Zhang, J. Gao, L. Sun, J.G. Hou, Engineering MoOx/MXene hole transfer layers for unexpected boosting of photoelectrochemical water oxidation, Angew. Chem. Int. Ed. 61 (2022) 6 e20220094.

[66] A. Vijeta, C. Casadevall, S. Roy, E. Reisner, Visible-light promoted C–O bond formation with an integrated carbon nitride–nickel heterogeneous photocatalyst, Angew. Chem. Int. Ed. 60 (2021) 8494–8499.

[67] Y.Y. Liu, D. Liang, L.Q. Lu, W.J. Xiao, Practical heterogeneous photoredox/nickel dual catalysis for C–N and C–O coupling reactions, Chem. Commun. 55 (2019) 4853–4856.